

Atmospheric Turbulence Compensation of Point Source Images Using Asynchronous Stochastic Parallel Gradient Descent Technique on AMOS 3.6 m Telescope*

M. Vorontsov^{1,4,5}, Jim F. Riker², G. Carhart¹, V. S. Rao Gudimetla³, L. Beresnev¹ and T. Weyrauch⁴

1. U. S. Army Research Laboratory, 2600 Powder Mill Road, Adelphi. MD, 20783-1197 (mvorontsov@arl.army.mil)
2. U. S. Air Force Research Laboratory, Directed Energy Directorate, Optics Division, 3550 Aberdeen Ave SE, Kirtland AFB, NM 87117
3. U. S. Air Force Research Laboratory, Directed Energy Directorate, Det. 15, 535 Lipoa Parkway, Keesler, MS 39063
4. University of Maryland, College Park, MD 20742
5. Corresponding author, mvorontsov@arl.army.mil

* This research work was funded by HEL-Joint Technology Office, Albuquerque, NM

Abstract

The Stochastic Parallel Gradient Descent Technique-based Adaptive Optics (SPGD-AO) system described in this presentation does not use a conventional wavefront sensor. It uses a metric signal collected by a single pixel detector placed behind a pinhole in the image plane to drive three deformable mirrors (DMs). The system is designed to compensate the image for turbulence effects. The theory behind this method is described in detail in [1]. However this technique, while widely simulated and tested in the laboratory, was not yet verified in astronomical field site experiments. During the month of May 2007, a series of experiments with SPGD-AO compensation on stars at several elevation angles and turbulence levels were conducted successfully at the US Air Force Maui Optical and Supercomputing Site (AMOS) using the 3.6 m telescope. Some of the results of these experiments are described in this paper. This is the first time SPGD-AO systems have been tested and verified in astronomical field site experiments.

1. Introduction

In imaging of astronomical objects located at high elevation angles, atmospheric turbulence can be considered to be a thin pupil-plane distorting layer that affects only the received wave phase - the so-called low-scintillation optical wave propagation regime. The phase aberrations introduced by this pupil-plane turbulence layer can be mitigated using conventional (astronomical) AO compensation techniques based on wavefront sensor measurements [2]. These measurements are used for computation of the control signals applied to wavefront corrector (deformable or segmented mirror) actuators [3].

For propagation through volume (deep) turbulence typical for observation of low elevation angle space objects, this conventional AO approach can be inefficient mostly because of the following two factors. First, wave propagation in volume turbulence commonly results in strong intensity scintillations leading to an increase of the noise level in wavefront sensor measurements and the appearance of errors in control signal computation [4-6]. Second, the intensity scintillations may result in discontinuities in the received wavefront phase known as wavefront dislocations (branch-points) [7-9]. These phase singularities are difficult to approximate and hence compensate using conventional

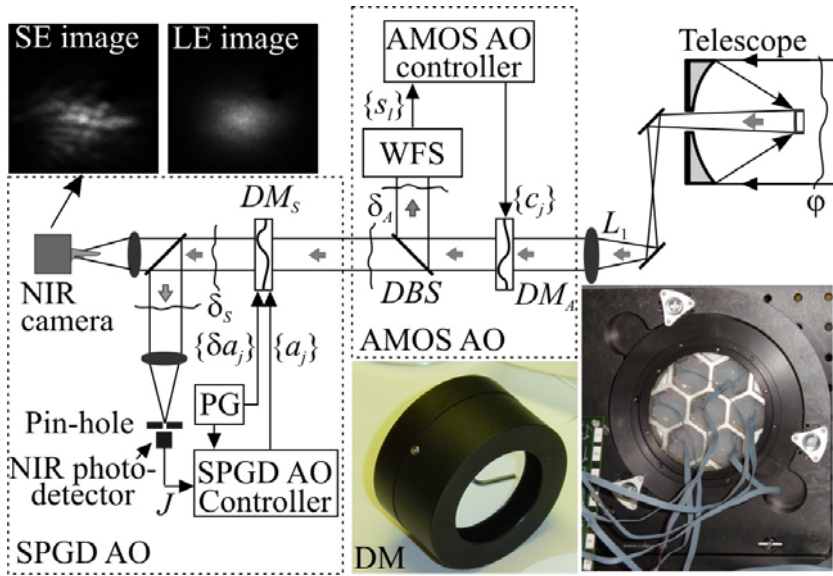


Fig. 1. Notional schematic of the cascaded AO imaging system and examples of short-exposure (SE image) and long-exposure (LE image) images of a star (Antares at 14 deg) obtained with NIR science camera without AO systems. Pictures at right bottom show two adaptive mirror types used in the SPGD AO system: 13-electrode bimorph DM (left) and 49-electrode pocket mirror (PM).

wavefront correctors - continuously deformable (DMs) or segmented adaptive mirrors. Compensation of deep turbulence effects therefore remains one of the most challenging problems for adaptive optics.

The major focus of the experimental AO compensation campaign discussed in this paper is adaptive compensation over long, near horizontal propagation paths using both a conventional AO system based on a Shack-Hartman wavefront sensor referred to here as AMOS AO, and the new adaptive optics technique which doesn't require measurements of wavefront phase characteristics (slopes, local curvatures, etc.) known as stochastic parallel gradient descent [1,10]. This new adaptive system is referred to here as SPGD AO.

The SPGD AO technique was proven to be more resilient to

intensity scintillations than the conventional AO technique but requires significantly higher operational bandwidth due to the iterative nature of the control algorithm [11-13].

The results presented provide the very first direct comparison of these two wavefront control approaches in various atmospheric conditions with the main emphasis on compensation of volume turbulence effects.

The near horizontal propagation regime in these experiments was achieved by imaging of stars at low elevation angles when image quality improvement with the conventional AMOS AO system was poor. Note that in all experiments performed using stars at high elevation angles, the AMOS AO system provided near-diffraction-limited image quality which could not be achieved with the SPGD AO system alone. However, in the experiments with the low-elevation stars, the SPGD AO system was able to demonstrate significant image quality improvement.

The most general conclusion derived from the experiments described is that there is significant benefit to using both conventional and SPGD adaptive optics techniques operating simultaneously in a cascade. The experimental results presented provide the first convincing arguments for the future development a new generation of adaptive optics techniques: Cascaded High-resolution Adaptive Optical Systems (CHAOS).

2. Experimental Setup of Cascaded Adaptive Optics System

A block diagram of the experimental setup is shown in Fig. 1. The adaptive imaging system is composed of the 3.6m telescope (AMOS) and two cascaded AO systems (the AMOS AO and SPGD AO systems). For convenience of graphical representation, wavefront correctors in both AO systems are shown as transmissive optical elements (DM_A and DM_S) while in the actual system only reflective optical elements were used.

The AMOS AO system is composed of the deformable mirror DM_A of diameter 100 mm with 941 actuators, the Shack-Hartman wavefront sensor (WFS) and the control electronics (AMOS AO

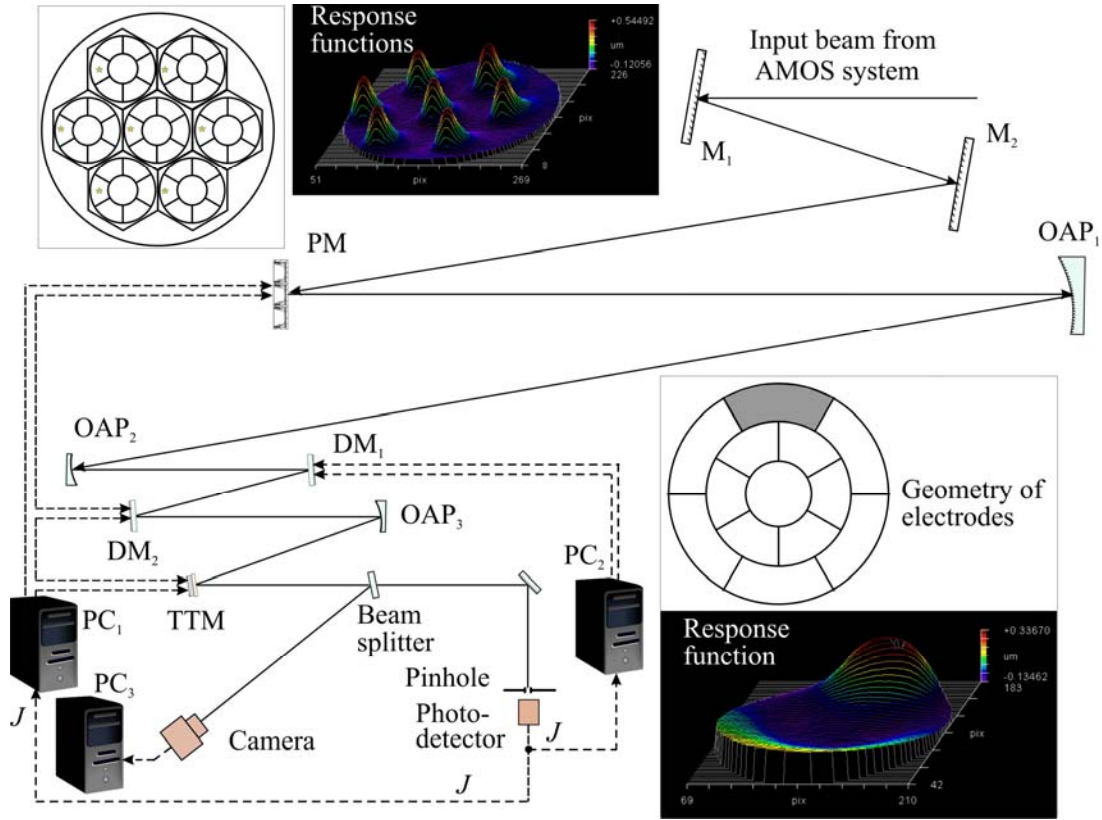


Fig. 2. Schematic of the SPGD AO system: M_1 and M_2 are flat mirrors, PM is pocket mirror, OAP_1 - OAP_3 are off-axis parabolic mirrors, DM_1 and DM_2 are bimorph deformable mirrors, TTM is tip-tilt (beam steering) mirror, PC_1 and PC_2 are SPGD controllers, and PC_3 is the image acquisition processor. The insert on top left shows geometry of electrodes of the pocket mirror (left) and the response functions corresponding to 50 volts applied to the electrodes marked by stars. The insert on bottom right shows geometry of electrodes of the bimorph DM (top) and the response function corresponding to 100 volts applied to the top electrode (shaded).

controller). The deformable mirror DM_A is located in the image of the telescope pupil plane. The AMOS AO system operated in the visible wavelength band. Compensation of the residual phase aberrations by the SPGD AO system was performed in the near infrared (NIR) band (0.9 - 1.7 microns). The dichroic beam splitter (DBS) reflected visible light to the AMOS AO wavefront sensor used to control the deformable mirror DM_A . The light in the NIR wavelength bandwidth passed this beam splitter and entered the SPGD AO system as shown in Fig. 1.

The SPGD AO system was located on an optical table in one of the AMOS Coude rooms. The optical axis of the SPGD AO system was carefully aligned with the AMOS telescope. The optical beam of diameter 100 mm corrected by the AMOS AO system passed through the set of four controllable mirrors of the SPGD AO system indicated in Fig. 1 as a single phase correcting element (DM_S). The corrected wave then entered a beam splitter (BS). A portion (~50%) of the light was used to record short-exposure (integration time 4 msec) corrected images of the star using a NIR camera from Sensors Unlimited Inc. The light reflected from the beam splitter entered the metric sensor. This sensor is composed of a lens with a small pinhole located in its focal plane. A single pixel photo-detector from New Focus Inc. with an active area 1x1 mm was used to measure the light power that passed through the pinhole.

The power P received by this photo-detector was used as a measure of the SPGD AO performance (performance metric) referred to also as the power-in-the-bucket metric. The output voltage J of the photo-detector used is proportional to the logarithm of received power P , so that $J=c \log(\alpha P+P_0)$,

where c , α and P_0 are coefficients dependent on the photo-receiver bias voltage and the signal amplification coefficient. The metric signal J was sent to the SPGD AO controller and was used to compute the control voltages $\{a_j\}$, $j=1, \dots, N$ applied to all wavefront corrector electrodes (total $N=75$ control channels).

3. SPGD Adaptive Optical System

The SPGD AO optical system schematic is shown in Fig. 2. The input optical beam was reflected from two 6" flat mirrors (M_1 and M_2) and then reflected from the pocket deformable mirror (PM). This mirror was located approximately in another image plane of the telescope pupil. The optical reducer composed of the off-axis parabolic mirror pair (OAP_1 and OAP_2) re-imaged the plane of the pocket mirror onto the first deformable mirror (DM_1) with four-fold demagnification. The optical beam (aperture diameter 25 mm) then propagated to the second deformable mirror (DM_2). After reflecting from the second deformable mirror, the optical beam was directed to another off-axis parabolic mirror (OAP_3) with the focal distance equal 40".

The focused beam propagated first to the plane of a flat mirror mounted on a tip-tilt platform (TTM) located at distance 13" from the OAP_3 mirror. The tip-tilt mirror was included for automated steering of the focal spot for alignment purposes as well as tip-tilt compensation when the AMOS AO tracking system was not used. In most cases we used the AMOS tracking system, and the tip-tilt control system was only used for alignment purposes. Finally, the convergent beam was divided with a beam splitter and split into two beams. The wave reflected by the beam splitter formed the image of the star at the fast framing NIR camera located in the focal plane of the OAP_3 mirror. The image of the star was recorded with frame rate 220 frames/sec and spatial resolution of 256x256 pixels. The pixel size was 25 μm , and the camera fill factor was 100%.

The portion of the convergent beam transmitted through the beam splitter was focused onto a pinhole placed in the second focal plane. The photo-detector was located approximately 3 mm behind the pinhole. In the experiments we used pinholes of three different diameters: 100 μm , 150 μm and 200 μm . The diffraction limited focal spot size (Airy spot diameter) was 90 μm . The metric signal (J) measured by the photo detector was used to close all control loops.

In experiments with the SPGD AO system, the following three wavefront correctors were used: one pocket deformable mirror (PM) of diameter 100 mm and two nearly identical deformable mirrors (DM_1 and DM_2) of diameter 25 mm. All three deformable mirrors are based on semi-passive piezo-ceramic bimorph elements and were designed and manufactured at the ARL Intelligent Optics Laboratory [14,15].

The pocket mirror was used for compensation of low-order aberrations inside seven densely packed hexagonal regions (pockets) machined into a 25 mm thick glass blank [6]. Deformation of the PM surface inside each pocket results from voltages applied to the electrodes of the piezo-ceramic disk. The discs are attached to the pocket mirror blank with silver deposited on the front surface. In Fig. 2 (insert at top left) the geometry of the 49 electrodes of the PM and an example of response functions are shown.

The deformable mirrors DM_1 and DM_2 are designed for compensation of low-order aberrations. The geometry of the 13 electrodes of these DMs and an example of a response function are shown in Fig. 2 (insert at bottom right). The electrodes are also patterned on a thin piezo-ceramic disc but attached to a thin (1.5 mm) glass plate with deposited gold layer. The deformable mirrors were mutually rotated by 30 degrees about the optical axis to minimize overlapping of their response functions. The bandwidth of the wavefront correctors used was near 12 kHz for the deformable mirrors DM_1 and DM_2 and 15 kHz for the pocket mirror.

The deformable mirror DM_1 was intended for compensation of atmospheric turbulence-induced large-scale aberrations. The optical train of the SPGD AO system had a static phase error on the order

of 0.6 μm (peak-to-valley value) that was composed mostly of defocus and astigmatisms. The second deformable mirror (DM₂) was originally intended for compensation of this static phase error to preserve full dynamical range of the first deformable mirror for compensation of solely atmospheric turbulence. Nevertheless in the course of our experiments we realized that this system phase error is slowly changing in the range of near 1.0 μm . We believe that these changes are related to quasi-static phase errors resulting from rotation of the AMOS telescope during star tracking and from wind pressure on the dome.

To compensate this quasi-static aberration we used an additional SPGD control loop, referred to here as the atmospheric-averaged SPGD control. The atmospheric-averaged control was based on measurements and averaging of 100 values of metric J performed with the time delay $\Delta t=0.1$ sec which significantly exceeds the characteristic time τ_{at} of atmospheric turbulence change. The atmospheric-averaging control was used to find the shape of the deformable mirror DM₂ prior to turning on the main (fast) SPGD control by maximizing the averaged value of the performance metric $\langle J \rangle$. After metric $\langle J \rangle$ is optimized the corresponding control voltages on the deformable mirror DM₂ were fixed and used as initial conditions for the “fast” SPGD control. This allows accurate estimation of image improvement associated with solely atmospheric turbulence compensation.

The second function of the deformable mirror DM₂ was to add more capabilities in spatial resolution and dynamical range for atmospheric turbulence compensation. In this regime both DM₁ and DM₂ were used for atmospheric aberration compensation with maximum possible speed. Both mirrors were driven by two independent and asynchronously operated SPGD controllers using identical metric J . The asynchronous SPGD control approach is described in [5].

4. SPGD Control System

The control system consisted of two SPGD controllers (PC₁ and PC₂) based on Dell desktop PCs (a 3GHz Dimension 8300 and a 3GHz Optiplex GX260) each equipped with Measurement Computing analog input cards and United Electronics Industries analog output cards. The Dimension PC controlled both the PM and DM₁ wavefront correctors operated as a single 62-channel SPGD AO control system (or a 13-channel or 49-channel SPGD AO system if using only one of these two correctors). A set of high-voltage amplifiers was used to amplify control signals to the range [-100v, 100v]. The Dimension PC also controlled the tip-tilt mirror when used for alignment purposes.

The Optiplex controlled the deformable mirror DM₂ operated as an independent (asynchronous) 13-channel SPGD AO system. The weak mutual impact of both SPGD AO systems on each other when both are operating simultaneously and asynchronously has previously been analyzed [5] and is here demonstrated experimentally.

In both SPGD AO systems (PM+DM₁ or DM₂) the control voltage update was performed using the following iterative update rule [4]

$$a_j^{(n+1)} = a_j^{(n)} + \gamma^{(n)} \delta a_j^{(n)} \delta J^{(n)}, \quad (j = 1, \dots, N), \quad n=1, \dots, \quad (1)$$

where $\delta a_j^{(n)} = \kappa^{(n)} \delta p_j^{(n)}$ is a small amplitude voltage perturbation applied to the deformable mirror (DM or PM) j th actuator at the n th iteration, and $\kappa^{(n)}$ is the perturbation amplitude, $\gamma^{(n)}$ is the gain coefficient, and $\delta J^{(n)}$ is the metric perturbation. Here $\{\delta p_j^{(n)}\}$ are a pre-calculated set of random numbers with zero mean and Bernoulli (coin-type) probability distribution. A second option for the perturbations was the use of a set of random numbers with zero mean and probability distribution corresponding to an approximation of Kolmogorov phase screen realizations using Zernike coefficients [4]. For either SPGD AO system, the control voltage perturbations were simultaneously applied to all wavefront correctors actuators. The perturbations are used to calculate the metric perturbation $\delta J^{(n)}$. In

the implemented version of the SPGD algorithm, the gain coefficient $\gamma^{(n)}$ and the perturbation amplitude $\kappa^{(n)}$ were functions of the current metric value $J^{(n)}$ [1,13]:

$$\gamma^{(n)} = \gamma_{\max} \left(\frac{J_{opt}}{J_{opt} + J^{(n)}} \right)^p, \quad \kappa^{(n)} = \kappa_{\max} \left(\frac{J_{opt}}{J_{opt} + J^{(n)}} \right)^q \quad (2)$$

where J_{opt} is the *a priori* expected optimum metric value, γ_{\max} and κ_{\max} are the maximum values the gain and perturbation amplitude coefficients are permitted to take, and p and q are numbers controlling the rate of decrease (with increasing $J^{(n)}$) of the two functions. Use of these functions to scale the gain and perturbation amplitude causes the SPGD AO system to use large perturbations and gains when the current metric is significantly less than the expected optimum value J_{opt} and smaller ones when it is near the optimum value (large perturbations and updates are not desirable if correction is achieved). Each of the different deformable mirrors had its own version of the four parameters p , q , γ_{\max} and κ_{\max} so their behavior could be adjusted independently.

With the control hardware used the maximum iteration rate for the SPGD controller with both 13-electrode deformable mirror DM₁ and the 49-electrode pocket mirror (PM) was near 7000 iteration per second, while the iteration rate of the second SPGD control system with the 13-electrode deformable mirror DM₂ was near 10000 iterations per second.

5. AO Compensation: Operational Regimes and Data Analysis

The experiments with the cascaded AO system were performed from May 17 until May 30, 2007 between 8:30 p.m. and midnight. As light sources for imaging we used several stars bright in the near infrared bandwidth: the first magnitude stars Antares (HR #6134) and Arcturus (HR #5340) observed respectively at elevation angles between 8 degrees and 30 degrees, and 50 degrees and 80 degrees and the third magnitude star Yed Prior (HR #6056) at near 45 degrees elevation.

Viewing conditions were changing from night to night and during the observation time. The compensation performance using both AMOS AO and the SPGD AO was very much dependent on these changing observation conditions as well as on the elevation of the imaging star. For this reason the parameters of the SPGD AO were optimized several times during the night to achieve the best possible image quality improvement. Clouds and strong wind during several observation nights resulted in poor performance of both AO systems, but when nights were clear, excellent data were collected.

It was possible to turn on and off the AMOS AO system during experiments and thus proceed with measurements corresponding to the following operational regimes:

1. **OFF/OFF** regime. Both AMOS AO and the SPGD AO controllers are off.
2. **ON/OFF** regime. The AMOS AO system is on and the SPGD controllers are off.
3. **OFF/ON** regime. The AMOS AO feedback controller is off, and the feedback loop of the SPGD system that includes the deformable mirror DM₁ and the pocket mirror PM is on.
4. **ON/ON** regime. AMOS and SPGD controllers are on.

Note that prior to the SPGD AO operation (**OFF/ON** and **ON/ON** regimes) we used the atmospheric-average SPGD optimization of the metric $\langle J \rangle$ as described in Section 3. This allows us to find control voltages $\{u_j^{aver}\}$, ($j=1, \dots, 13$) for the second deformable mirror (DM₂) corresponding to pre-compensation of static phase aberrations. These voltages were fixed during the SPDS system operation.

Adaptive optics system performance estimation and control parameter optimization were based on the following procedure referred to here as the *adaptation trial*. The adaptation trial was composed of a large number M of the SPGD iterations (40000 or 80000) that lasted about 4 or 8 seconds and included the following subsequent phases that lasted $M/4$ iterations each:

- (a) **SPGD_OFF** phase. During this phase the SPGD controller was off and the voltages on both the PM and DM₁ were fixed.
- (b) **PM_ONLY** phase. In this phase the SPGD controller updated only the control voltages applied to the pocket mirror and the voltages on DM₁ were fixed.
- (c) **DM_ONLY** phase. In this phase the control voltages on the PM were fixed and the SPGD controller updated only 13 control voltages of DM₁.
- (d) **SPGD_ON**. During this phase the SPGD controller updated voltages on both DM₁ and the PM wavefront correctors.

During the adaptation trial the metric values $J(m)$ measured at each SPGD iteration m , ($m=1, \dots, M$) were recorded. Because the actual adaptation rate was also recorded, the temporal behavior of the optimized metric $J(t)$ can be easily obtained from the dependence $J(m)$.

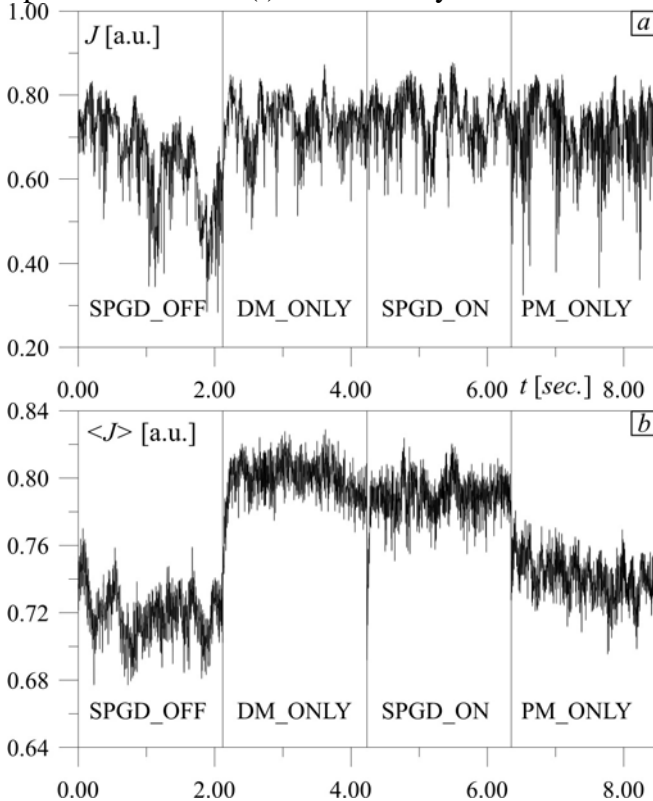


Fig. 3. Characteristic examples of metric J time dependence corresponding to a single (a) and averaged (b) adaptation trials composed of four adaptation phases. The pinhole size is equal 150 micron. Light source was Antares at elevation angle 16 deg. The AMOS AO system was on.

A typical adaptation trial $J(t)$ is shown in Fig. 3 a. Continuous changes in the atmospheric turbulence conditions resulted in strong variations in the adaptation trials.

To decrease dependence on varying atmospheric conditions, a large number (typically ~ 30) of sequential adaptation trials were averaged. An example of the averaged adaptation curve $\langle J(t) \rangle$ is shown in Fig. 3 b. The averaged curve shows obvious improvement achieved by using the SPGD controller. Note that the metric J is logarithmically dependent on the received power inside the pinhole. Note also that in the adaptation trials shown in Fig. 3, the best performance was achieved in the DM_ONLY phase, when the SPGD control was used to drive solely the deformable mirror DM₁ with static voltages applied to the pocket mirror. This efficiency decrease in the SPGD_ON phase, when compared with the DM_ONLY phase, was quite typical and can be explained by both non-optimal parameters

for the PM SPGD loop, and a 15%-20% decrease in the adaptation rate that occurred when the additional 49 channels of the pocket mirror were included in the SPGD feedback loop since a single computer was used to drive both the deformable and pocket mirrors. Note that in the computation of time dependences we used an

averaged iteration rate, and hence this decrease in the adaptation rate is not accounted for in Fig. 3 and other figures below. This decrease in the adaptation rate can be avoided by having independent asynchronously operating SPGD processors for the deformable and pocket mirrors. Even so in some cases we did observe noticeable improvement when the PM was included in the SPGD feedback loop together with DM.

Also during the adaptation trials we computed four metric histograms, $h(J)$, corresponding to each of the four operational phases. Here h is the number of events that occurred during the corresponding adaptation phase for which the measured metric value belonged to the interval $[J, J+\Delta J]$. The metric interval ΔJ (metric bin) corresponded to 1/512th of the entire dynamical range in metric signal

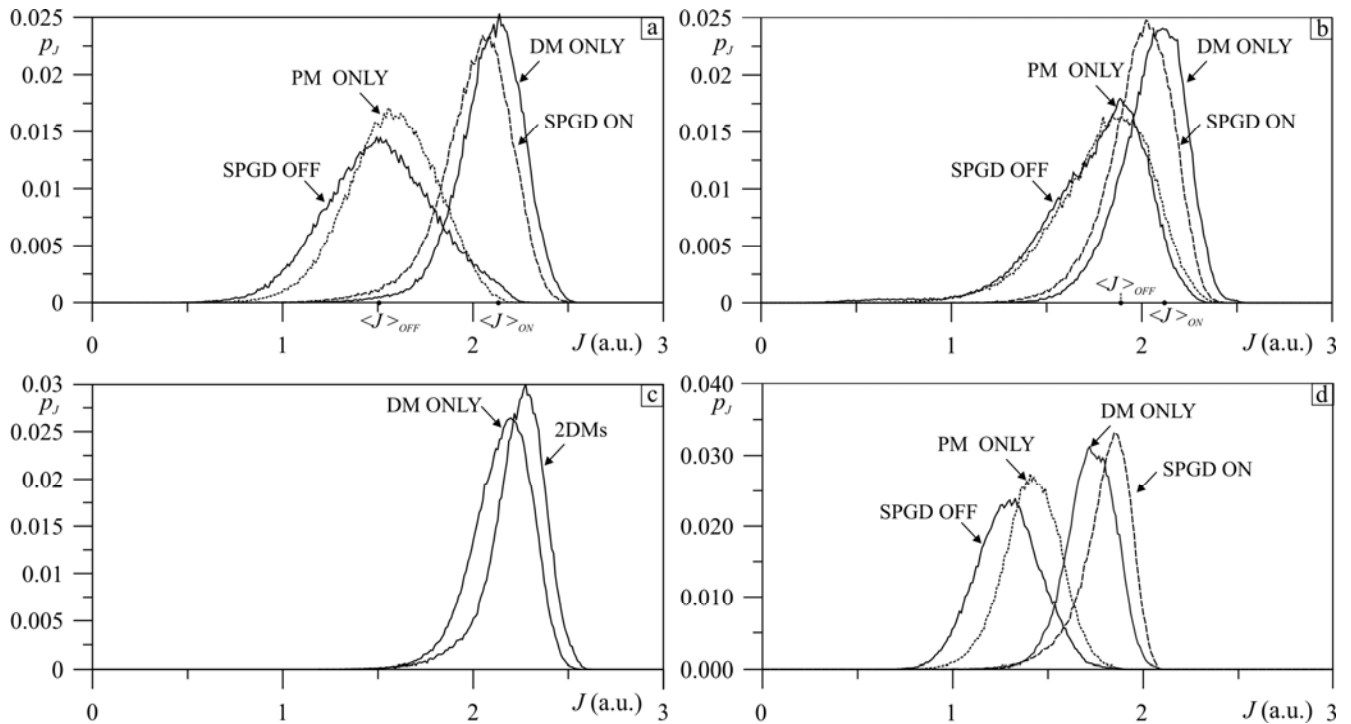


Fig. 4. Probability distribution of the power-in-the-bucket metric J obtained by collection of 50 adaptation trials: (a) without and (b) with quasi-static (atmospheric averaged) phase error compensation; (c) with SPGD controller operating with one or two of the deformable mirrors DM_1 and DM_2 ; (d) an example of adaptive system operation which shows the advantage of using both deformable and pocket mirrors together. The corresponding data were recorded with AMOS AO off using Antares as a light source at elevation angle between 16-18 degrees (between 9:09 p.m. and 9:30 p.m.) on May 18, 2007 (a-c) and on May 17 (d). The SPGD adaptation rate was about 6000 (a,b,d) or 8000 (c) iterations per second. The pinhole size for metric measurements was 200 microns.

measurements. Averaged over the large number of adaptation trials, histograms $p_J(J) = \langle h(J) \rangle$ characterize the probability distribution of metric values in the four different adaptation phases. The averaged histograms $p_J(J)$ were typically computed using about 10^6 metric measurements. The data collection lasted about 3 or 6 minutes (depending on the M value used and the adaptation rate).

Examples of the metric histograms corresponding to the four phases of the adaptation trials with AMOS AO off are presented in Fig. 4 a, b. The histograms in Fig. 4 a were obtained using as an initial condition (the voltages applied to the deformable and pocket mirrors at the beginning of each adaptation trial phase) the voltages obtained by optimizing metric J using a reference light source (light beam from a Zygo interferometer).

The data presented in Fig. 4b shows the same metric histograms for the initial conditions obtained using an atmospheric-average metric optimization similar to that described in Section 3. In order to “track” the quasi-static aberrations we used a voltage set for both the pocket and deformable mirrors at the beginning of each phase of the adaptation trial that was a set of average voltages obtained during the SPGD_ON phase of the previous adaptation trial. This procedure uses an “average” correction corresponding to the previous adaptation trial. The initial voltage set for most of the histograms collected was obtained with this procedure. Comparison of these histograms shows clearly that the initial conditions play an important role in the true estimation of the atmospheric compensation efficiency.

Compensation of the quasi-static aberrations resulted in the increase of the averaged metric value $\langle J \rangle_{OFF}$ corresponding to the point of the histogram (probability) maximum. Compare points $\langle J \rangle_{OFF}$ and $\langle J \rangle_{ON}$ in Fig. 4 a, b.

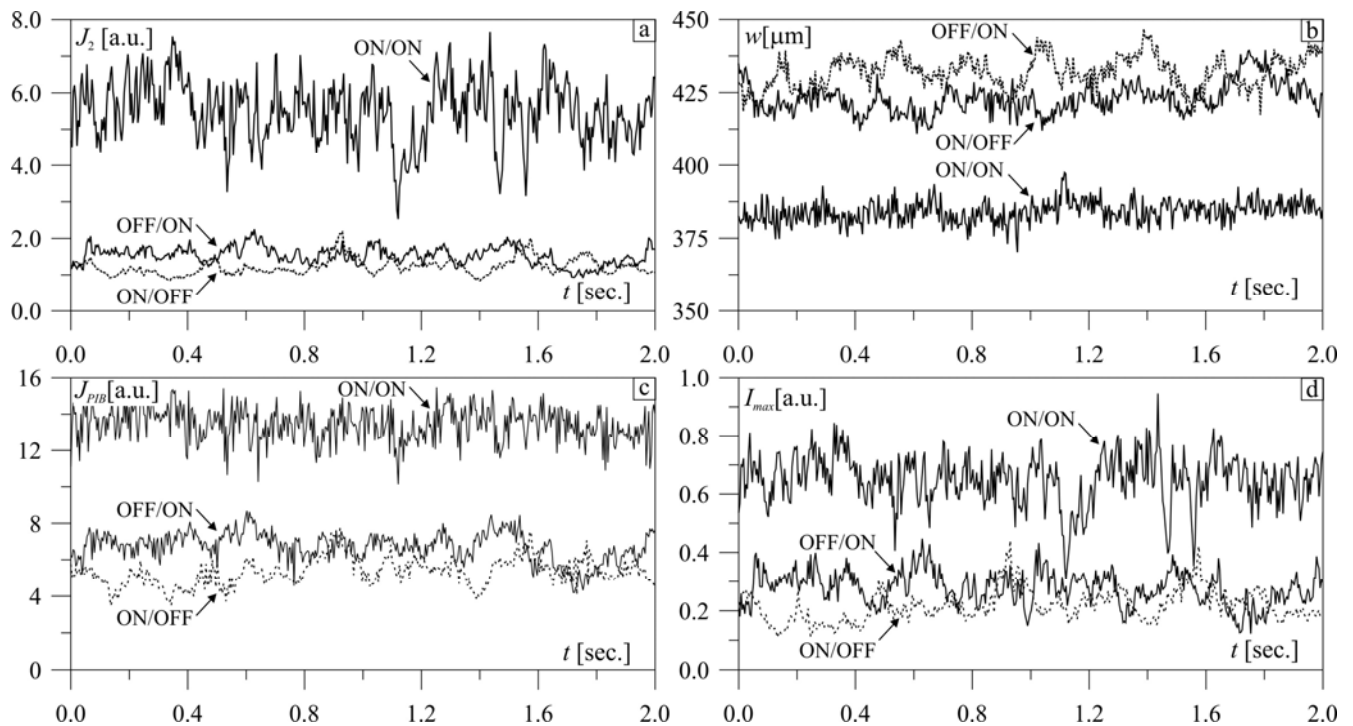


Fig. 5. Temporal dependences of the image quality metrics calculated based on post-processing of video-sequence (movie) containing 500 short-exposure near IR images of the 3d magnitude star at near 45 degree elevation angle for the following SPGD AO operational regimes: ON/ON (feedback control of both AMOS AO and SPGD AO with DM₁ and PM), OFF/ON (control of only SPGD AO) and ON/OFF (control of only AMOS AO). The image quality metrics J_2 (sharpness function) in (a); power in the circular area of 200 microns in (c); and maximum image intensity in (d) are shown in arbitrary units [a.u]. The image width in (b) is measured in microns. The diffraction limited beam diameter is 90 microns. The movies were recorded on May 18, 2007. The SPGD adaptation rate was 4600 iterations per second. The pinhole size was 200 microns.

The histogram width characterizes metric J fluctuations. As seen from Fig. 4 a,b adaptive compensation not only results in the increase of the averaged metric value $\langle J \rangle_{ON}$ that corresponds to the histogram maximum, but also leads to histogram narrowing – an indication of the decrease of the metric value fluctuations. In these examples voltages on the second deformable mirror (DM₂) were fixed and corresponded to either optimal voltages obtained by optimization of metric J using reference source (a) or using the atmospheric average metric $\langle J \rangle$ with the star as light source (b).

A characteristic example of the SPGD compensation results using two deformable mirrors DM₁ and DM₂ is shown in Fig. 4 c. Both mirrors were driven asynchronously with the iteration rates 6000 and 9000 iterations per second respectively. As seen from these histograms, use of two deformable mirrors (curve 2DMs) resulted in the average metric increase and decrease of the metric fluctuations.

Comparison of the adaptation phases DM_ONLY and SPGD ON in Fig. 4 a,b shows that the best performance was achieved when only the deformable mirror DM₁ was active, and the voltages on the pocket mirror were fixed. The histograms in Fig. 4 d provides an illustration the observed cases when the SPGD feedback control which included both the deformable and pocket mirrors resulted in better performance than the SPGD control using the deformable mirror only (compare curves DM ONLY and SPGD ON in Fig. 4 d).

6. Selected Experimental Results

Consider now the adaptation results obtained with fast-framing CCD NIR camera located in the image plane of the SPGD AO system as shown in Fig. 2. The imagery data (movies representing a set of 500 short-exposure images recorded with the frame rate 220 frames per second) is an independent

information source for adaptive system performance evaluation. The movies were recording in the different operational regimes mentioned above (OFF/OFF, OFF/ON, ON/OFF and ON/ON). Post processing of the movies allowed us to obtain the following independent image quality metrics:

- (a) Power-in-the-bucket metric $J_{PIB}(d)$, and (b) the power outside the bucket $J_{PIB}^{out}(d)$ - received power area at the camera sensor inside or outside a circular of diameter d centered with the image centroid. In the case when the diameter d equals the diameter of the pinhole, the metric $J_{PIB}(d)$ is similar to the metric J actually measured. The difference is that the metric $J_{PIB}(d)$ is directly proportional to power inside the pinhole (bucket) but the sensor used for SPGD control J depends on this power logarithmically.
- (c) Sharpness function J_2 defined as the integral of the squared intensity over imaging chip area S .
- (d) Image width w defined as

$$w^2 = \frac{1}{P_0} \int_S |\mathbf{r} - \mathbf{r}_c|^2 I(\mathbf{r}) d^2\mathbf{r}, \text{ where } \mathbf{r}_c = \frac{1}{P_0} \int_S \mathbf{r} I(\mathbf{r}) d^2\mathbf{r} \quad (3)$$

is image centroid vector, and P_0 is the integral of image plane intensity over sensor area, referred to here as received light power.

- (e) Point-source image maximum intensity I_{max} . Examples of image quality metric calculations based on processing of short-exposure image stream (movie) for the third magnitude star Yed Prior (HR #6056) at near 45 degrees elevation are presented in Fig. 5 for different adaptation regimes. Note the use of either the AMOS AO or SPGD AO system alone resulted on average in a relatively small (near 30%) improvement of the image quality as measured by the sharpness function J_2 , while use of both adaptive systems in a cascade (ON/ON regime) led to near three times increase of the sharpness function value (Fig. 5 a), decrease of the image width from near 425 microns to near 380 microns (Fig. 5b), two fold increase of the power in the bucket metric and in peak intensity value (Fig. 5c,d).

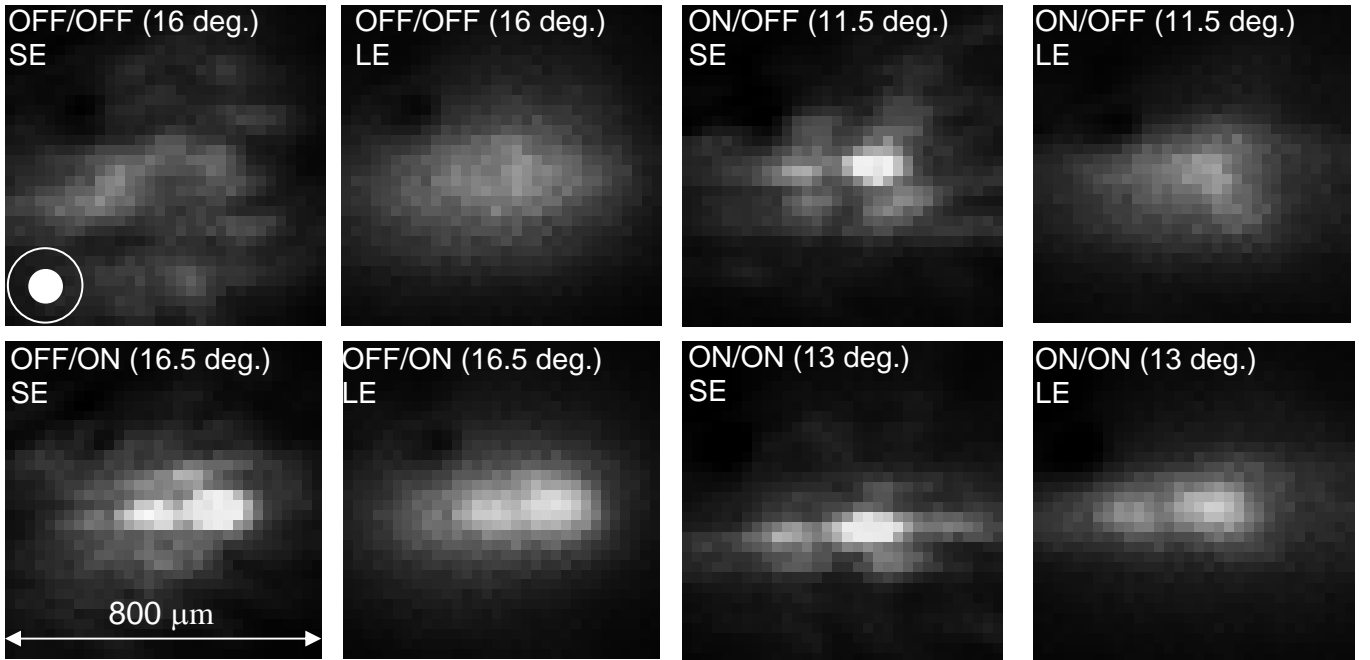


Fig. 6. Short- (SE) and long- (LE) images of the star Antares at low elevation angles (numbers in parentheses) obtained in the cascade adaptive optical system with operational regimes (OFF/OFF; OFF/ON; ON/OFF and ON/ON) on May 18, 2007. The diffraction-limited image and the pinhole sizes are shown in the upper left photo by white circle and ring respectively.

Analysis of the recorded imagery data shows that at low elevation angles images of stars were commonly distorted nonuniformly, which we relate with the existence of rising laminar air flows close to the telescope dome. The examples of both short-exposure and frame averaged (long-exposure) images of the star Antares at elevation angles between 11-deg. and 17-deg. are shown in Fig. 6. The experiments conducted in May 2007 resulted in considerable amounts of this kind of truth-sensor data, along with the histogram metric data $\langle J \rangle$ discussed earlier. There are numerous Technical Engineering Memoranda (TEM) published locally containing synopses of all these data collects, including the conditions during the tests (ref. 16). We continue to analyze these data for presentation in a more complete form such as a journal article, but that will occur after the data analysis is complete. For this paper, we simply wished to illustrate the basic optical design and the sample results shown above. The upshot of all these results is that SPGD has now been demonstrated in the field to significantly improve both the Strehl ratio surrogate (the pinhole measurement) and the image quality on stars in a repeatable way even in the presence of stressing atmospheric conditions obtained on low-elevation stars at AMOS.

7. Bibliography

1. M.A. Vorontsov, M. A., and V. P. Sivokon, "Stochastic parallel gradient descent technique for high-resolution wavefront phase distortion correction," *J. Opt. Soc. Am.*, **15**, 2745-2758, (1998).
2. J. W. Hardy, *Adaptive Optics for Astronomical Telescopes* (Oxford University Press, New York, 1998).
3. F. Roddier, *Adaptive Optics in Astronomy* (Cambridge University Press, New York, 1999).
4. M. Chen, F. S. Roux, and J. C. Olivier, "Detection of phase singularities with a Shack-Hartmann wavefront sensor," *J. Opt. Soc. Am.*, **24**, 1994-2002, (2007).
5. J. D. Barchers, D. L. Fried, and D. J. Link, "Evaluation of the performance of Hartmann sensors in strong scintillation," *Appl. Opt.* **41**, 1012-1021, (2002).
6. M. C. Roggemann and A. C. Koivunen, "Wave-front sensing and deformable-mirror control in strong scintillation," *J. Opt. Soc. Am. A* **17**, 911-919, (2000).
7. D. L. Fried, "Branch point problem in adaptive optics," *J. Opt. Soc. Am. A* **15**, 2759-2768, (1998).
8. G. A. Tyler, "Reconstruction and assessment of the least squares and slope discrepancy components of the phase," *J. Opt. Soc. Am. A* **17**, 1828-1839, (2000).
9. V. P. Aksenov and O. V. Tikhomirova, "Theory of singular-phase reconstruction for an optical speckle field in the turbulent atmosphere," *J. Opt. Soc. Am. A*, **19**, 345-355, (2002).
10. M. A. Vorontsov, G. W. Carhart and J.C. Ricklin, "Adaptive phase-distortion correction based on parallel gradient-descent optimization," *Opt. Lett.* **22**, 907-909, (1997).
11. M. A. Vorontsov, G. W. Carhart, M. Cohen and G. Cauwenberghs, "Adaptive optics based on analog parallel stochastic optimization: analysis and experimental demonstration," *J. Opt. Soc. Am. A*, **17**(8), 1440-1453 (2000).
12. T. Weyrauch, M. A. Vorontsov, T. G. Bifano, Jay Hammer, M. Cohen, and G. Cauwenberghs, "Micro-scale adaptive optics: wavefront control with μ -mirror array and VLSI stochastic gradient descent controller," *Applied Optics*, **40**, Aug. N 24, 4243-4253, (2001)

13. T. Weyrauch and M. A. Vorontsov, "Atmospheric compensation with a speckle beacon under strong scintillation conditions: directed energy and laser communication applications," *Applied Optics*, **44**, N. 30, pp. 1-14, (2005)
14. L. A. Beresnev, M. A. Vorontsov, and P. Wangsness, "Pocket deformable mirror for adaptive optics applications," AMOS Technical Conference, Maui HI, September 2006: AMOS Proceedings, pp.568-575. (2006).
15. L. A. Beresnev, M. A. Vorontsov "Scalable-size deformable pocket mirror with on-pockets bimorph actuators," provisional Patent Application to the United States Patent and Trademark Office (USPTO), filed 2006.
16. Riker, J.F., Vorontsov, M., and R. Gudimetla, TEM 20070507r0-060: Stellar radiometry for JTO atmospheric turbulence project on an IR camera, TEM 20070507r0-061: First light operations for JTO atmospheric compensation, TEM 20070508r0-062: JTO atmospheric compensation for 8 May 2007, TEM 20070509-065: JTO atmospheric compensation for 9 May 2007, TEM 20070510-067: JTO atmospheric compensation for 10 May 2007 – SPGD closed loop, etc. (total of 15 TEMs).